# Large Eddy Simulation and Laser Doppler Velocimetry on a vortex flow meter model

Olle Penttinen[a,*], Håkan Nilsson[b]

[a] *SP Technical Research Institute of Sweden, Box 857, SE-501 15 Borås, Sweden*
[b] *Chalmers University of Technology, SE-412 96 Göteborg, Sweden*

**Abstract**

The present work compares the results from a Large Eddy Simulation (LES) and the result of two Laser Doppler Velocimetry (LDV) measurements. The work focuses on a model of a vortex flow meter, a common flow meter type in process industry. Its measuring principle is that the frequency of a vortex street, generated by a shedder bar, is acquired by pressure or velocity sensors. The shedding frequency is proportional to the bulk flow rate. Tests are performed at a Reynolds number of 61400, based on the pipe diameter. A complementary LDV measurement is also performed at a Reynolds number of 62800. All results are normalized with the bulk velocity to be comparable to each other. A comparison of the mean streamwise velocity profiles shows excellent agreement between the numerical and experimental methods. The variance of the two velocity components is also in good agreement between the investigated results. It is shown that it is possible to capture the vortex shedding frequency by analysis of primary LDV data at the investigated Reynolds number. Velocity fluctuations due to secondary vortices are highlighted both in the LES and LDV results. Post-processing of the frequency spectra is implemented utilizing Bayesian probability theory which strengthens the dominating frequencies and attenuates the noise. The fundamental shedding frequencies found by numerical and experimental methods are shown to be within the limits of theoretical estimations. The redundant results strengthens the reliability of each individual method.

The results from flow simulations and measurements are associated with uncertainties. The different types of uncertainty contributions are described and the results are evaluated taking calculated uncertainty contributions into account. For the LDV cases, estimated uncertainty contributions from the test setup, are included in the end results.

*Keywords:* large eddy simulation; laser doppler velocimetry; vortex flow meter; Bayesian theory; measurement uncertainty;

[*] Corresponding author
*Email addresses:* olle.penttinen@sp.se (Olle Penttinen), hakan.nilsson@chalmers.se (Håkan Nilsson)

*May 13, 2015*

## 1. Introduction

A vortex flow meter consists of a bluff body, positioned in a pipe section. At high enough Reynolds numbers, a von Kármán [1] vortex street is created downstream the bluff body. The frequency of such a von Kármán vortex street is proportional to the mean velocity of the surrounding fluid. This proportionality is used in vortex flow meters. Due to its widespread usage, and to the transient flow it creates, it is chosen as a suitable object for the present work, where the results from numerical and experimental methods are compared.

Comprehensive reviews of numerical and experimental vortex flow meter related research is presented by Pankanin [2] and Venugopal et al. [3]. The importance of boundary layer control on the bluff body, to achieve a stable signal, is highlighted. Achenbach [4] noticed an oscillation of the boundary layer up to the stagnation point when examining flow around a cylindrical rod. Boundary layer control is accomplished by a well defined separation point, i.e. sharp edges, of the bluff body. Hans et al. [5] and Hans and Windorfer [6] show that orientating a triangular bluff body, called a shedder bar, with one side facing the flow, give rise to secondary vortices. Zhang et al. [7] compares Unsteady Reynolds Averaged Navier-Stokes (URANS) simulations to experiments with differential pressure transducers. Zhang et al. get numerical and experimental results with good agreement regarding the shedding frequency, though a fixed value boundary condition for the inlet velocity is used in the numerical procedure. In the experimental results for water, there are signs of harmonics present in the frequency spectra for the lower velocities, which indicates an energy contribution from secondary vortices. There are however no indication of secondary vortices in their numerical results.

In the present work, Large Eddy Simulation (LES) is utilized instead of URANS, to enhance the possibilities of secondary vortex prediction. LES is preferable when it comes to studying unsteady flow phenomena like von Kármán vortex streets. LES is expected to give more accurate results than URANS simulations, due to higher mesh resolution and less modelling.

Laser Doppler Velocimetry (LDV) is one of the most accurate measuring techniques to determine the fluid velocity through a well defined measurement volume. Velocity measurements are also more prone than piezoelectric transducers to be susceptible to the small fluctuations originating from e.g. secondary vortices [6].

The present work presents the results from one numerical LES, at a Reynolds number of, $Re_D = 6.14 \times 10^4$, where $D$ is the pipe diameter, $Re_d = 1.43 \times 10^4$, where $d$ is the hydraulic diameter of the shedder bar. These results are compared to experimental results from LDV measurements performed at the flow facilities of SP[1], Sweden, for the same geometry at identical Reynolds numbers. Complimentary LDV results are acquired from the flow facilities of PTB[2], Germany, at $Re_D = 6.28 \times 10^4$, corresponding to $Re_d = 1.46 \times 10^4$. A vortex flow meter model is constructed, consisting of a shedder bar mounted in a glass pipe. The glass pipe enables optical access for the LDV. Measurements are performed downstream the shedder bar.

The results are compared in terms of the mean streamwise velocities with corresponding uncertainty values. The variance of the spanwise and streamwise velocity components are compared between the numerical and experimental results. Instantaneous fields of velocity, pressure and vorticity are presented from the numerical results. The acquired vortex shedding frequencies of the numerical and experimental results are derived and compared to theoretical values based on the mean velocity profile and the Strouhal number.

[1] SP Technical Research Institute of Sweden
[2] PTB Physikalisch-Technische Bundesanstalt

Section 2 describes the test case. Section 3 gives descriptions of the numerical and experimental methods. The results are presented in Section 4, while the conclusions are found in Section 5.

## 2. Test case description

Section 2.1 gives a detailed description of the object investigated in the present work. Section 2.2 describes the compared cases.

### *2.1. Test object*

A model of a vortex flow meter is constructed. Figure 1 shows a CAD drawing of the model. A triangular shedder bar is welded to two supporting flat bars which in turn are welded to a

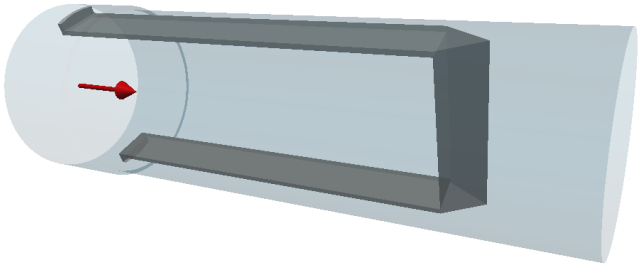

Fig. 1: CAD drawing of the investigated vortex flow meter model. The flow direction is indicated by an arrow. The view has been restricted in the streamwise direction to enhance visibility.

supporting stainless steel flange. This construction is inserted into a glass pipe. The assembly is concentrically connected to a stainless steel pipe with flanges of the same dimensions in the upstream direction. The inner radius of the glass pipe is 4.7% smaller, than the upstream pipe, since it was originally used in another work. Hence, there is a small forward facing step in the streamwise direction in connection to the attachment points of the supporting arms. The flange is specified as DN100, PN16 according to DIN[3] standards.The shape of the shedder bar is carefully selected to ensure a stable separation point. Venugopal et al. [3] stated that an ideal bluff body should have sharp edges to be independent of the Reynolds number. Hence, the object of the present work is a triangular equilateral iron bar, with sharp edges of 60°. Each side has a length of $d = 0.23D$, where $D$ is the pipe inner diameter. The assembly makes it possible to perform optical measurements of the flow in an object which to a large extent resembles the inside of a vortex flow meter.

### *2.2. Compared cases*

The present work compares results from three different investigations, as shown in Table 1. The first investigation is a LES at $Re_D = 6.14 \times 10^4$. Two LDV studies are also carried out. The first one is performed at SP, Sweden. The input to the LES simulation, i.e. the viscosity, $\nu$, and bulk flow, $U_b$, is identical with those of *SP*, which is why these two cases have an identical

[3]Deutsches Institut für Normung

Table 1: Cases compared in this work.

| Case | $Re_D$ | $Re_d$ | $\lvert u\rvert$ [a)] | $\overline{u}_x$ | $\sigma^2(u_x)$ | $\sigma^2(u_y)$ | $u'_y$ |
|---|---|---|---|---|---|---|---|
| *LES* | $6.14 \times 10^4$ | $1.43 \times 10^4$ | x [b)] | x | x | x | x |
| *SP* | $6.14 \times 10^4$ | $1.43 \times 10^4$ | - [c)] | x | x | - | x |
| *PTB* | $6.28 \times 10^4$ | $1.46 \times 10^4$ | - | x | x | x | - |

a) All variables are normalized with the bulk velocity, $U_b$.
b) x: Shows that the quantity is included in the investigated case.
c) -: Shows that the quantity is not included in the investigated case.

$Re_D$. The third case represents complementary measurements carried out on the same object at PTB, Germany. It has a slightly higher $Re_D$ due to differences in $\nu$ and $U_b$. The *LES* case is investigated both in terms of streamwise mean velocity, $\overline{u}_x$, as well as the variance in streamwise and spanwise direction, $\sigma^2(u_x)$ and $\sigma^2(u_y)$ respectively. The frequency content of the sampled signal, $u'_y$, is also calculated. For the *SP* case, $\sigma^2(u_y)$ was not acquired. For the *PTB* case, the investigation of $u'_y$ is excluded. Table 1 summarizes the extracted data for each case. All data are normalized by the streamwise bulk velocity, $U_b$.

## 3. Methodology

The numerical procedure is described in Section 3.1 while Section 3.2 gives a general overview of the numerical methods. Section 3.3 describes the experimental methods.

### *3.1. Numerical procedure*

Section 3.1.1 describes the computational domain and includes a motivation of the selection of the inlet boundary condition. Section 3.1.2 gives a background to the analysis of mean values. Section 3.1.3 describes the transient analysis.

#### *3.1.1. Computational domain and mesh*

The computational domain represents a pipe section with an inserted shedder bar, see Fig. 1. The dimensions match the physical model used in the experimental measurements, described in Section 2.1. A Cartesian coordinate system is used, where $\hat{\boldsymbol{x}}$ represents the streamwise direction. Origo is located at the intersection of the pipe centreline and the downstream facing edge of the triangular shedder bar. The inlet is positioned $7.89D$ upstream origo, while the outlet is positioned $6.55D$ downstream origo. In total, the computational domain consists of $1.63 \times 10^7$ hexahedra cells. The block structured o-grid around the shedder bar and the supporting arms enables a well defined cell concentration within the important boundary layers.

The inlet boundary condition is *mapped*, which means that the instantaneous velocity from an internal plane downstream from the inlet is mapped to the inlet. It enables the flow to develop both in terms of average profiles and turbulence. To ensure a negligible correlation between the inlet and the mapping plane, the length between the inlet and the mapping plane is chosen based on the results from a LES of undisturbed pipe flow, shown in Fig. 9. The undisturbed reference

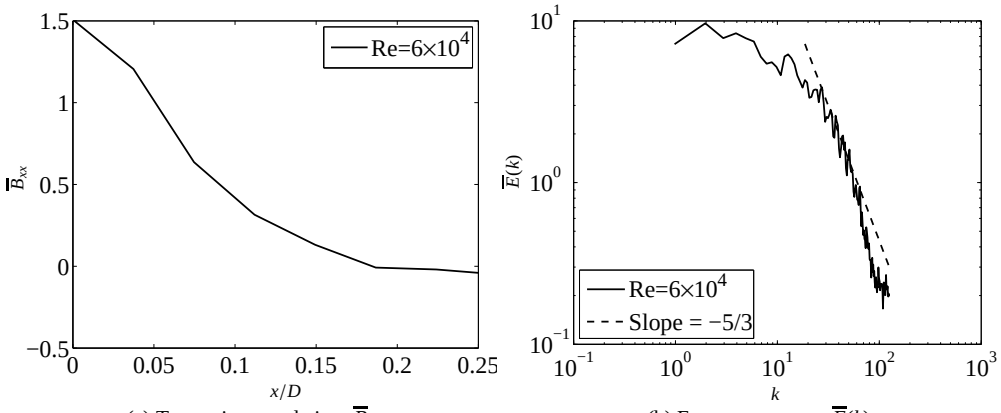


(a) Two-point-correlation, $\overline{B}_{xx}$. (b) Energy spectrum, $\overline{E}(k)$.

Fig. 2: Undisturbed pipe flow at $Re_D = 6 \times 10^4$.

case has a domain length of $10D$ and consists of $8.2 \times 10^6$ hexahedra cells and the Reynolds number is $Re = 6 \times 10^4$. Figure 2(a) shows that the two-point-correlation drops rapidly for low separation distances $x/D$. The two-point-correlation, $\overline{B}_{xx}$, is negligible for a normalized separation distance of $x/D \geq 0.2$. A distance between the inlet and the mapping plane of $3D$ is chosen to ensure that any correlation is extinguished. The total distance from the inlet to the mounting points of the model is $6D$, to avoid an uneven pressure distribution from the blockage caused by the model to propagate upstream, into the mapped region. The energy spectrum of Fig. 2(b) shows that the simulation of undisturbed flow is well resolved, since it has a characteristic profile compared to the $-5/3$-slope, representing the *Kolmogorov* decay. Hence, a proper transport of energy through the turbulent scales is established.

### *3.1.2. Mean profiles*

The calculations are performed with a time step, $\Delta t = 5 \times 10^{-5}$ s. The corresponding average $CFL$-number [8] is $CFL_{avg} = 0.01$, while the maximum $CFL_{max} = 0.6$ in the vicinity of the separation point at the edge of the triangular shedder bar. The instantaneous velocity components, $u_x$ and $u_y$, are sampled every time step at the same positions as the measurements, described in Section 3.3.2. Data from the first 8 s simulation time is excluded to make sure that stable conditions are reached. The data is averaged from $t_{start} = 8$ s to $t_{end} = 20$ s, which corresponds to 2.9 flow-through times. The mean profile of the *LES* case is defined as

$$\overline{u}_{x,LES}(\boldsymbol{x}_i)/U_b = \frac{1}{N}\sum_{j=1}^{N} u_{x,LES}(\boldsymbol{x}_i, t_{start} + j\Delta t), \tag{1}$$

where $N$ is the number of samples and $\boldsymbol{x}_i$ is the probe position. The mean profile of the streamwise velocity component, $u_{x,LES}$, is normalized with the bulk velocity, $U_b$. The numerical results are presented with an uncertainty. The reported uncertainty, $\upsilon$, is defined by the normalized standard uncertainty of the mean,

$$\upsilon(\overline{u}_{x,LES}) = \pm k\frac{\sigma(u_{x,LES})}{\sqrt{N}}, k = 2, \tag{2}$$

where $N$ is the number of observations in each point $\boldsymbol{x}_i$. The coverage factor $k = 2$, yields a level of confidence of approximately 95%. Estimated uncertainty contributions due to selection of turbulence model, selection of boundary conditions and mesh effects, are excluded deliberately. The estimation of these types of uncertainties in numerical studies is an active area of research [9, 10].

*3.1.3. Transient analysis*

The transient analysis of the *LES* case is based on data from one probe. That probe is located at the pipe centre, $x/d = 0.4$ downstream of the backward facing edge of the triangular rod. The position is chosen to enable comparison of the results to the acquired experimental data, described in Section 3.3.2. A robust locally weighted regression method, originating from Cleveland [11], is used to smoothen the spanwise velocity fluctuations. The robust method is not influenced by a small number of outliers within the computational span, which has a width of 0.1 s. This operation enhances the visibility of the fundamental vortex shedding and simplifies identification of secondary vortices. The calculation of the vortex shedding frequency is however performed based on unfiltered data. The expected shedding frequency is approximated by

$$f_{St} = \frac{St \cdot v}{d} \tag{3}$$

where $St = 0.26$ is the expected Strouhal number for a triangular body in free stream, $v$ is the velocity and $d$ the diameter of the shedder bar. The triangular shape makes $St$ fairly insensitive to changes in $Re$, due to its stable separation point. In a confined space however, as in the present work, $f_{St}$ is expected to be dependent of the distance to the wall. White [12] gives an approximation of the relationship between maximum velocity, $u_{max}$, and mean velocity, $U_b$, for turbulent pipe flow in smooth pipes as

$$u_{max} = \left(1 + 1.3\sqrt{\phi}\right)U_b. \tag{4}$$

Colebrook [13] approximates the the friction factor, $\phi$, as

$$\phi = \left(1.8 \log \frac{Re_D}{6.9}\right)^2. \tag{5}$$

Since $f_{St} \propto v$, the shedding frequency is expected within a range of $3.86 \leq f_{St} \leq 4.57$ Hz, where the lower limit is given by $v = U_b$ and the higher by $v = u_{max}$ inserted into Eq. 3.

The triangular shedder bar orientation is optimized for signal detection by pressure transducers that are either located at the shedder bar itself or at the pipe wall. Measurements and simulations of velocity fluctuations in the present orientation are susceptible to secondary vortices, which interfere with the primary vortices of the vortex street [6]. Since the number of oscillations is fairly limited due to the relatively short simulation time, the acquired data is post-processed carefully. Hence a moving average is utilized when performing a Fast Fourier Transform (FFT), as described by Welch [14]. To resolve the low frequencies, a minimum time frame of 5.025 s is chosen. The data within each time frame is convoluted with a Gaussian filter to reduce frequency leakage. Further improvement of the result is achieved by incorporating Bayesian theory.

Bretthorst [15] basically states that the posterior probability density for $f$ of a discrete data set, $D$, with variance $\sigma^2$, is given by

$$P(f|D, \sigma, I) \propto \exp\left\{\frac{C(f)}{\sigma^2}\right\}, \tag{6}$$

where $I$ is the prior information. $C(f)$ is the normalized result of the FFT, given by

$$C(f) = \frac{1}{N}|FFT|^2, \tag{7}$$

where $N$ is the number of observations. Equation. 6 gives a proportional relationship for the probability density of $f$, and the absolute magnitude is not of great importance in this work. Hence, the results are scaled to yield a maximum amplitude of unity for both the *LES* and the *SP* case. The Bayesian theory is incorporated to enhance the resonance frequency and suppress the noise of the acquired signals. The described method is also used for the experimental data.

### *3.2. Numerical method*

The simulations of the present work are performed with the OpenFOAM® open source CFD tool, which is based on the finite volume method. The temporal discretization is described in Section 3.2.1 and the spatial discretization of the convection term is described in Section 3.2.2. The pressure-velocity coupling is explained in Section 3.2.3.

#### *3.2.1. Backward differencing in time*

The backward temporal differencing scheme, used in the present simulations, is second-order accurate [16]. This scheme stores the values from two previous time steps, resulting in a larger data overhead than the standard first-order backward schemes [17]. The time term is thus discretized as

$$\frac{\partial}{\partial t}\int_V \rho\phi \, dV = \frac{3(\rho_P\phi_P V)^m - 4(\rho_P\phi_P V)^{m-1} + (\rho_P\phi_P V)^{m-2}}{2\Delta t}. \tag{8}$$

Superscript $m$ indicates the current time step.

#### *3.2.2. Central differencing in space*

The convection scheme is discretized using the second-order central differencing (CD) scheme [18]. In a 1D example, the face value, $\xi_f$, is calculated according to

$$\xi_f = \frac{|\boldsymbol{fN}|}{|\boldsymbol{PN}|}\xi_P + \left(1 - \frac{|\boldsymbol{fN}|}{|\boldsymbol{PN}|}\right)\xi_N. \tag{9}$$

The distance between the position of the cell centre, $\boldsymbol{P}$, and the neighbour cell centre, $\boldsymbol{N}$, is denoted $|\boldsymbol{PN}|$. The shortest distance between the cell face, $\boldsymbol{f}$, and the cell centre, $\boldsymbol{N}$, is denoted $|\boldsymbol{fN}|$.

#### *3.2.3. Pressure-velocity coupling*

The pressure-velocity coupling is realized by a PISO/SIMPLE-algorithm, also known as PIMPLE. The main part of the PIMPLE algorithm is inherited from the transient PISO-algorithm (Pressure Implicit with Splitting of Operators) by Issa [19], which originally was intended as a non-iterative approach to solve coupled pressure and velocity transport equations by splitting up the solution in several steps. It includes one predictor step, where initial values for the velocity field are approximated. Two subsequent solutions of the pressure correction equation yields the correct pressure field and updates the solution of the velocity field. In the non-iterative version of PISO, the corrections of the pressure and velocity fields are followed by a solution of the

transport equations for other scalar fields, such as turbulence quantities, and the solution is considered to be reached at that time step. This requires very short time steps to keep the accuracy. The steady-state SIMPLE-algorithm (Semi-Implicit Method for Pressure-Linked Equations) by Patankar and Spalding [20] iterates over the solution of the momentum equations, the pressure correction equations, and the turbulence equations, until convergence is reached. In the SIMPLE algorithm, the variables are under-relaxed according to

$$\xi^{m+1} = \alpha\xi^{m} + (1-\alpha)\xi^{m-1}, \tag{10}$$

which improves convergence. Here, $\xi$ symbolizes an arbitrary variable. Index $m$ defines the current time step. The relaxation factor, $\alpha$, may be specified in the interval $0 < \alpha < 1$. The PIMPLE algorithm is based on the PISO algorithm, but introduces an outer correction loop and under-relaxation in accordance with the SIMPLE algorithm. The simulations presented in this work are performed with three outer corrector loops at each time step.

*3.2.4. Turbulence model*

When using LES, the incompressible Navier-Stokes equations are filtered in space which results in

$$\frac{\partial \hat{v}_i}{\partial t} + \frac{\partial(\hat{v}_i\hat{v}_j)}{\partial x_j} = -\frac{1}{\rho}\frac{\partial \hat{p}}{\partial x_i} + \nu\frac{\partial^2 \hat{v}_i}{\partial x_k \partial x_k} - \frac{\partial \tau_{ij}}{\partial x_j}. \tag{11}$$

where the notation $\hat{}$ indicates a filtered variable. The filtered Navier-Stokes equations contain the subgrid-scale Reynolds stress tensor,

$$\tau_{ij} = \widehat{v_i v_j} - \hat{v}_i\hat{v}_j. \tag{12}$$

Since it represents stresses in the subgrid-scales, it can not be resolved, hence it needs to be modelled. The turbulence model invented by Smagorinsky [21],

$$\begin{aligned} \tau_{ij} &= 2\mu_{sgs}\hat{S}_{ij} + \frac{1}{3}\tau_{ii}\delta_{ij}, \\ \hat{S}_{ij} &= \frac{1}{2}\left(\frac{\partial \hat{u}_i}{\partial x_j} + \frac{\partial \hat{u}_j}{\partial x_i}\right), \\ \mu_{sgs} &= C_S^2\rho\Delta^2|\hat{S}| \end{aligned} \tag{13}$$

is used in the present work. Equation 13 includes the local rate of strain, $\hat{S}_{ij}$, and the subgrid-scale eddy viscosity, $\mu_{sgs}$. $\Delta$ is the filter length scale. The Smagorinsky constant is set to $C_S = 0.1$ for pipe flow [22, 23]. In the present work, van Driest damping has been used to further reduce the SGS Reynolds stress near the solid boundaries.

*3.3. Experimental method*

Section 3.3.1 contains a summary of the hardware in the LDV system. Details of the measuring plan is described in Section 3.3.2

*3.3.1. LDV setup*

The core of the primary LDV system at SP consists of a Melles-Griot Series 543 argon air-cooled ion laser system [24]. One channel is used in the present work. The laser produces a monochromatic, coherent and highly collimated light beam which is split into a beam pair

with a base wavelength of $\lambda = 514.5$ nm. One of the beams is shifted by 40 MHz. Using a frequency shifted beam enables detection of low and negative particle velocities, which is important due to the expected recirculation region behind the shedder bar. The light beams are directed to an 83 mm fiberoptic probe which focuses the beams to the measuring volume within the glass pipe, shown in Fig. 3. The power output of the laser is adjustable between

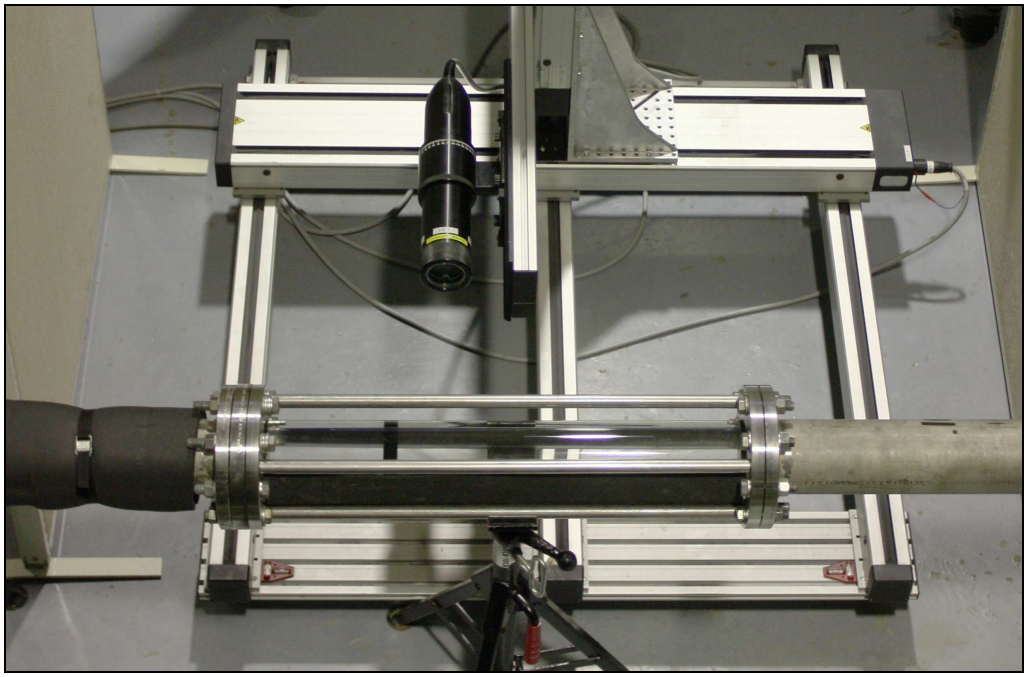

Fig. 3: Photograph of the fiberoptic probe, positioned in front of the glass pipe. Flow direction is from left to right.

300 – 750 mW. The beam diameter is 0.68 mm $\pm$ 5% and the beam divergence is stated to be 1.1 mm $\pm$ 5%. This corresponds to a beam quality measure of $M^2 = 1.2$. The corresponding measuring volume is estimated to 0.008 mm$^3$. The data acquisition is relying on a TSI PDM 1000-2 photo multiplicator [25] with a maximum frequency of 300 MHz. The A/D converter for the intensity measurement has a 12 bit resolution. The electrical signal from PDM 1000-2 is sent to a FSA 3500 Signal Processor, which extracts the frequency information from the electrical signal and transfers it by IEEE1394 (FireWire) to the controller. The system is controlled with the TSI FlowSizer$^{TM}$ software.

*3.3.2. Measurements*

LDV measurements are performed at two different laboratories. The primary measurements are performed at SP. These measurements are performed at $Re_D = 6.14 \times 10^4$, where $Re_D$ is the Reynolds number based on pipe diameter, $D$, corresponding to $Re_d = 1.43 \times 10^4$ based on the hydraulic diameter of the shedder bar, $d$. 45 positions are covered along the $x$-axis in a Cartesian coordinate system, $y = 0, z = 0$, i.e. along the centre of the pipe, as shown in Fig. 4. There is a higher concentration of measuring points close to the shedder bar, to capture the expected wake

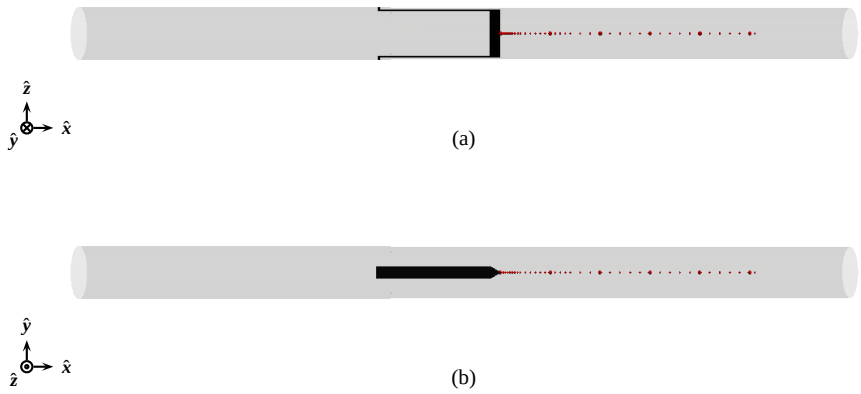


Fig. 4: The pipe section with the inserted shedder bar, shown in $\hat{\boldsymbol{y}}$ and $\hat{\boldsymbol{z}}$ directions. Probe positions indicated with red dots.

properly. The larger dots have an equidistant spacing of $4d$. A total measuring range downstream the back edge of the shedder bar of $0 < x/d < 20.4$ is covered. Measurements of the streamwise velocity component, $u_x$, are made at each position. The measurements are averaged during 120 s in each point. The standard deviations are calculated simultaneously. The measurements are performed twice with intermediate traversing to ensure measurement reproducibility and bulk flow stability. The bulk flow rate is measured with an inductive flow meter calibrated against a ball prover. The ball prover serves as the primary standard of the SP calibration facilities. The averaged bulk flow rate, $U_b$, acquired during the measurements is used as input to the LES, described in Section 3.1. Based on the calculated variance of the streamwise velocity, $\sigma^2(u_x)$, a suitable point of investigating the spanwise fluctuations, $u'_y$, is found to be at the end of the wake. Due to the sparse concentration of seeding in that region, the measuring volume is however positioned closer to the shedder bar, where the backward flow increases the number of particles. Hence, the focal point for $u'_y$-measurements is positioned at $x/d = 0.4$ downstream of the backward facing edge. This yields a good Signal to Noise Ratio (SNR), due to a beneficial balance between particle counts and velocity fluctuations. The post-processing of the unsteady LDV data is performed according to Section 3.1.3, though the time frame of the moving average, according to Welch [14], is set to 4.1 s.

Complementary LDV measurements are performed on the same model at PTB, in Berlin. These measurements are performed at $Re_D = 6.28 \times 10^4$, or $Re_d = 1.46 \times 10^4$. Since the Reynolds number is slightly different from that during the measurements at SP, all results are scaled with the bulk flow rate, to enable comparison of the measurements. At PTB, the bulk flow is simultaneously acquired with an inductive flow meter during the LDV measurements. Instead of the glass pipe used at SP, a glass chamber was used at PTB. The inner diameter of the glass chamber matches the inner diameter of the attached pipe, specified as DN100, PN16. Hence, the LES model does not fully resemble the measurement situation at PTB. The forward facing step is missing in that installation. As the results reveal, the influence of the pipe diameter is however negligible. The size of the chamber window at PTB restricts the downstream measuring range to $0 < x/d < 5.64$. Within that range, 27 probe positions are covered by both LDV measurements.

In these 27 positions, 8 reproduced measurements where carried out, with intermediate traversing. In the experimental cases, $\overline{u}_x$ and its corresponding standard deviation, $\sigma$, is given by the LDV systems. Since the measurements includes repetitive measurements at each probe position, the averaging of the experimental data is defined as

$$\overline{u}_{x,exp}(\boldsymbol{x}_i)/U_b = \frac{1}{M}\sum_{j=1}^{M} u\left(\boldsymbol{x}_{i,j}\right), \tag{14}$$

where $M$ is the number of repeated measurements in each point. The combined measurement uncertainty of $\overline{u}_{x,exp}$ is given by

$$\upsilon\left(\overline{u}_{x,exp}\right) = \pm k\sqrt{A^2 + B^2}, k = 2, \tag{15}$$

where capital Latin letters represent type $A$ and type $B$ uncertainties [26]. In this case, the type $A$ uncertainty refers to the normalized standard deviation, described by Eq. 2, though with coverage factor, $k = 1$. Type $B$ represents the estimated measurement uncertainty of the reference instrument, i.e. the LDV. In this case, 0.2% of the reading is added, based on ITTC [27]. The same number is used for both experimental set-ups, *SP* and *PTB*. The results are presented as an expanded uncertainty at a confidence level of 95%, coverage factor $k = 2$. It should be noted that this work does not include a comprehensive uncertainty budget for minor changes in ambient conditions and uncertainties originating from the flow rigs.

## 4. Results

The *LES* results are here compared to the experimental results of *SP* and *PTB*. Section 4.1 presents the instantaneous velocity and pressure fields of the *LES* case. Section 4.2 shows the results from comparisons between the numerical and experimental cases, regarding mean profiles of $u_x$ and standard deviation of $u_x$ and $u_y$. Finally, Section 4.3 shows the probability density functions of the frequency, $f$, for the *LES* and *SP* cases.

### *4.1. Instantaneous velocity and pressure fields*

An instantaneous flow field of the *LES* case is displayed in Fig. 5. Figure 5(a) shows the normalized velocity magnitude, $|u|/U_b$, in a plane with normal pointing in the $y$-direction, while Fig. 5(b) shows the same property in a plane with the normal in the $z$-direction. Both planes are laterally restricted in the streamwise direction to enhance visibility of the interesting regions close to the shedder bar. The visible range is $-4 < x/d < 20$, with origo located at the downstream facing edge of the triangular shedder bar as reference. Figure 5(a) shows that the blockage effect of the shedder bar forces the velocity to increase at the narrow slit between the arms of the model and the pipe wall. Due to the fragile glass pipe, the design was still chosen as the preferable solution. The data analysis focuses on the pipe centre line, where the influence from the model arms is negligible. Figure 5(b) shows that there is a stable and well-defined separation point at the edge of the triangular shedder bar. The triangular form of the shedder bar produces a distinctly separated flow. An instantaneous pressure field is shown in Fig. 6.

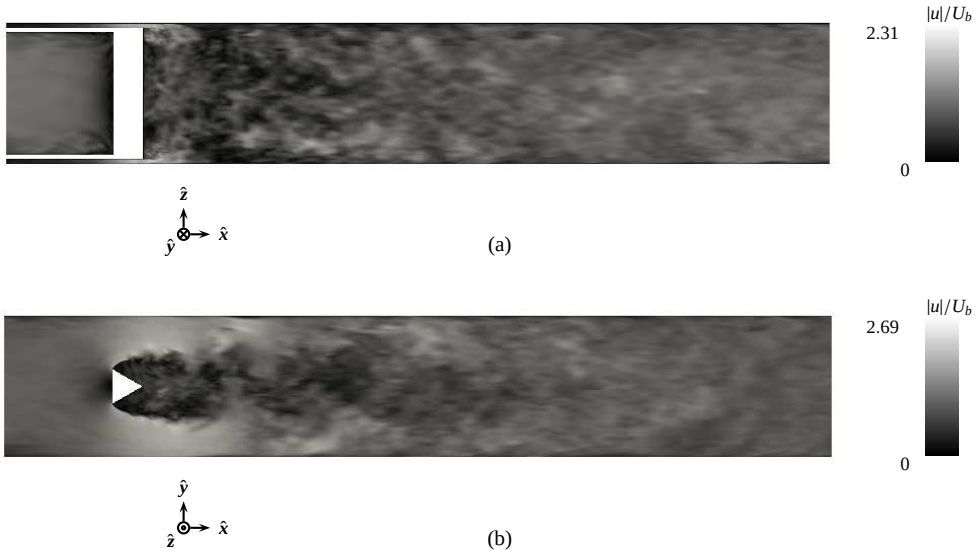


Fig. 5: Velocity magnitude at 20 s simulation time.

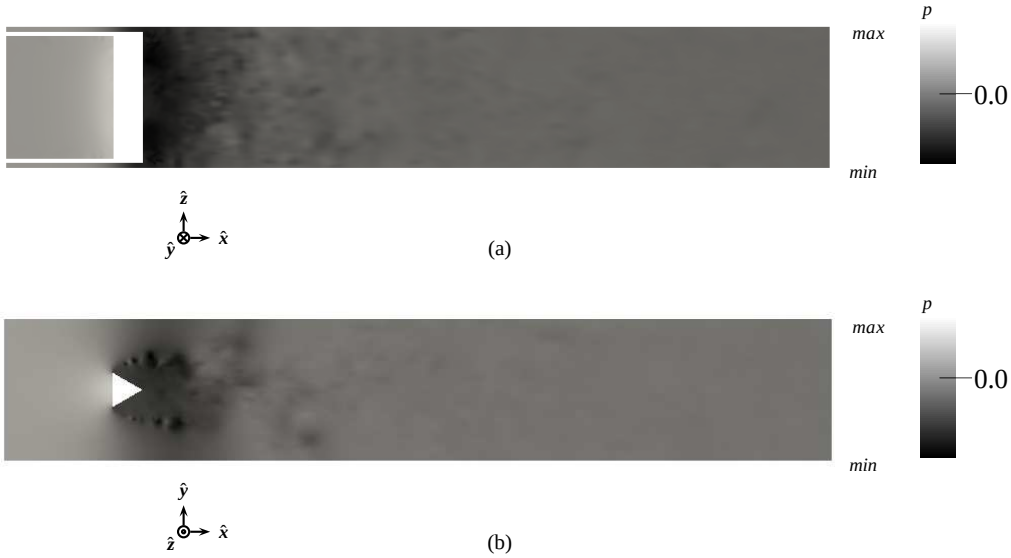


Fig. 6: Pressure distribution at 20 s simulation time.

The distinct pressure drop over the triangular shedder bar, as well as the downstream pressure recovery, is shown in Fig. 6(a). Figure 6(b) shows how the flow separation gives rise to strong corresponding pressure fluctuations located along the borders of separation. Compared to Fig. 5(b) the pressure fluctuations coincide with the distinct change of velocity magnitude be-

tween the separated flow and the recirculating region.

Hunt et al. [28] show that eddy zones are identified by defining regions where the second invariant, $II$, of the deformation tensor, $\partial u_i/\partial x_j$, is less than a negative threshold value. This is today slightly redefined as the $Q$-criterion, where positive values of $Q$ identifies vortex regions. For confined spaces, with strong vorticity, a high threshold of $Q$ is needed, to highlight the interesting areas. The correlation between the strong pressure gradients and the generation of vortices is clearly shown in Fig. 7. Here, half of the computational domain of the *LES* case

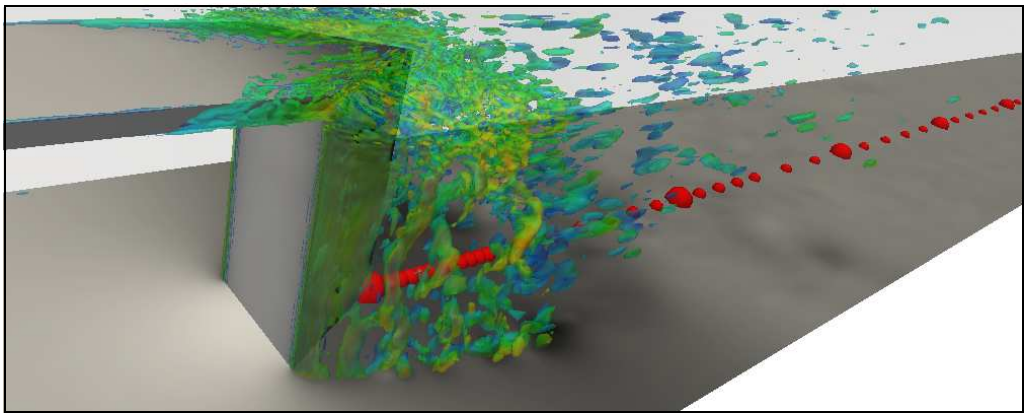

Fig. 7: Iso-surfaces of $Q = 1.5 \times 10^4$, colored with $|u|$. Half the computational domain is shown, i.e. $0 \leq z \leq D/2$. Geometry and symmetry surface coloured by $p$. Dots indicate probe positions.

is shown, i.e. $0 \leq z \leq D/2$. The dots indicate the probe positions. The semi-transparent pipe wall, the model and the horizontal cutting plane are coloured by the static pressure, $p$. Lower pressure regions are represented by darker shades. The iso-surface of $Q = 1.5 \times 10^4$ is coloured with the velocity magnitude, $|u|$. It is shown that correlated vortex structures originates from the separation region at the edge of the shedder bar. The vortex structures are coupled to the pressure minima, which are visualized in the horizontal plane, along the path of separation downstream. It is also shown that the fluid is forced towards the narrow slit above the supporting arm, due to a negative pressure gradient in that area. This is also visible in Fig. 5(a). The vortical structures are less coherent closer to the pipe wall. Hence, the best SNR is found at the pipe centre.

### *4.2. Mean profiles*

Figure 8 shows the mean profiles of the streamwise velocity, $\overline{u}_x/U_b$, along the centre line of the pipe, downstream the triangular shedder bar. The mean values are represented by dark curves. The gray curves represent the estimated uncertainty. It should be noted that the uncertainty estimation of the *LES* case only includes type *A* contributions. Since the number of observations, $N$, is large in the simulation compared to the experiments, the normalized deviation, $\sigma/\sqrt{N}$, is negligible. For the LDV measurements, the type *A* contribution is the dominating source for the combined measurement uncertainty. It is also noticed that the uncertainty estimation is relatively large, caused by the velocity fluctuations. Still, the agreement between the mean profiles of three cases is remarkably good. At no point is the mean value of the *LES* result outside the boundaries of the uncertainty estimates of the experimental cases. The differences in spatial measuring range is noted between the experimental *SP* and *PTB* cases, where the latter is restricted in the

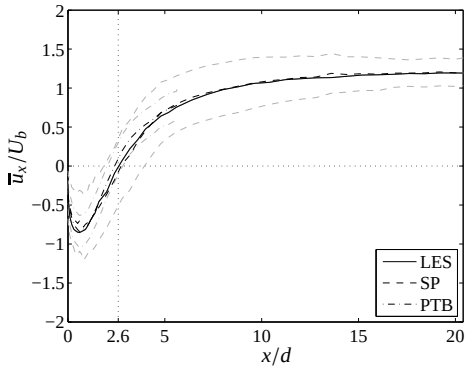


Fig. 8: Normalized average streamwise velocity, $\overline{u}_x/Ub$, in black, surrounded by uncertainty estimations in gray.

streamwise direction due to the size of the measuring chamber. Figure 8 also shows that the mean velocity is zero at a downstream distance from the shedder bar of $x/d \simeq 2.6$, which defines the end of the wake.

It is also of interest to compare the variance of the streamwise velocities directly, which gives an indication of the amount of turbulence. The variance of the instantaneous streamwise velocity, $\sigma^2(u_x)/U_b$, is shown in Fig. 9(a). It is shown that there is a good agreement between

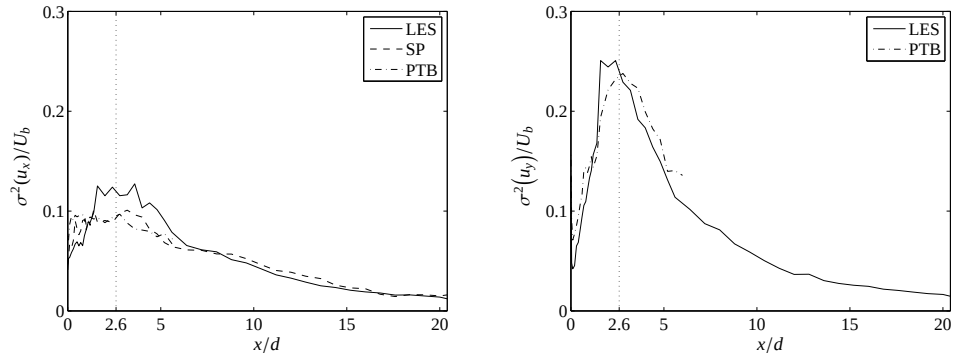


(a) Streamwise, $\sigma^2(u_x)/U_b$.

(b) Spanwise, $\sigma^2\big(u_y\big)/U_b$.

Fig. 9: Variance of velocity components

the numerical results and the results from the two experimental cases. It is also shown that the maximum of $\sigma^2(u_x)/U_b$ is located at $x/d \simeq 2.6$ which coincides with the zero crossing of $\overline{u}_x/U_b$ in Fig. 8. The slight overestimation of $\sigma^2(u_x)/U_b$ in the numerical result is explained by the stable bulk flow of the numerical case, which is further discussed in Section 4.3. For the results of the two experimental cases it is shown that some of the energy of the spanwise fluctuations is transferred closer to the downstream facing edge of the shedder bar. The results for the variance

of spanwise velocity, $\sigma^2\left(u_y\right)/U_b$, is missing from the *SP* case, according to Table 1. Hence, for $\sigma^2\left(u_y\right)/U_b$, a comparison is made between *LES* and *PTB*. The results are shown in Fig. 9(b). As shown, the *PTB* case captures the spanwise fluctuations really well, compared to the *LES* case. The results confirms the previous findings regarding the elongation of the wake.

### *4.3. Transient results*

An optimal position for a frequency measurement with LDV would be at the end of the wake, i.e. at $x/d \simeq 2.6$ since there is where the velocity fluctuations are largest, according to Section 4.2. However, the amount of seeding does not generate a high enough burst rate for the LDV measurement at that position. Instead, Fig. 10 shows a subset of the normalized spanwise velocity fluctuations, $u_y/U_b$, from probe data positioned at $x/d = 0.4$ downstream the backward facing edge of the shedder bar, along the centreline of the pipe. The spanwise velocity fluctuations in Fig. 10, are filtered according to Section 3.1.3. In the *SP* dataset, the velocity

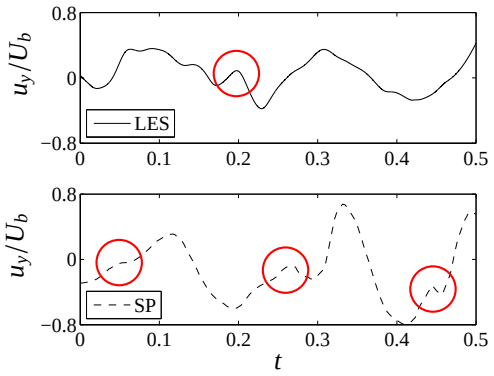


Fig. 10: Normalized spanwise velocity fluctuations, $u_y/U_b$, from the *LES* and *SP* results. Influences from secondary vortices are indicated by circles.

fluctuations due to the primary vortex shedding is clearly visible. The influence of secondary vortices is highlighted with circles. The primary fluctuations of the *LES* are not as distinct as in the *SP* dataset, but some influence of the secondary vortices are still visible.

The probability distributions from the probe data positioned at $x/d = 0.4$ is shown in Fig. 11. The energy contribution from the secondary vortices in the *SP* data results in a first harmonic, highlighted with a circle for consistency. For the *LES* case, a distinct first harmonic is not visible which is explained by the irregular appearance of secondary vortices in the *LES* data. For the spanwise velocity, $\sigma^2(0.4d) \simeq 0.08$. As stated in Section 3.1.3, $\sigma^2$ is used in the post-processing to enhance the properties of the probability distribution function $P(f,|D,\sigma,I)$. As mentioned in Section 3.1.3, the FFT:s are further processed through Bayesian theory to enhance the resonance frequency and suppress the noise. Both probability distributions have a large energy content at $f \leq 6$ Hz. They both have an amplitude peak within the theoretically estimated Strouhal frequency range, $3.86 \leq f_{St} \leq 4.57$ Hz, where the peak of the *LES* result is slightly more distinct. The probability density function for the experimental *SP* results, show more evenly distributed energy contents for $f < f_{St}$ compared to the *LES* result. This is due to the unavoidable instabilities of the flow rig during the measurements. Even though the uncertainty of the rig is exceptional, dynamic effects from upstream piping and inherent dynamics of the system will always affect

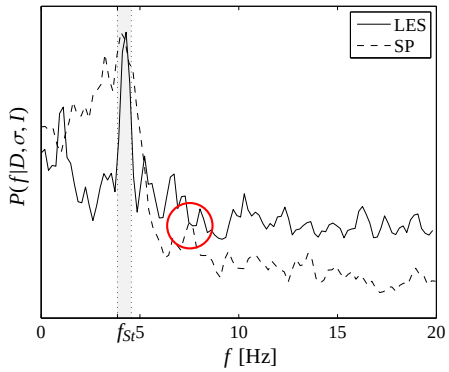


Fig. 11: Posterior probability density distributions of the *LES* and *SP* results. Influence from secondary vortices on the *SP* results is indicated with a circle.

the results. Here it can be seen as an additional energy contribution to the low frequencies of the *SP* result. The stability of the flow rig can not be compared to the stability of the *LES* setup, in which the inlet boundary condition has been adjusted to yield the average bulk velocity, $U_b$, at each time step.

## 5. Conclusions

A Large Eddy Simulation (LES) is performed, of turbulent flow through a vortex flow meter model at a Reynolds number of $Re_D = 6.14 \times 10^4$, based on the pipe diameter $D$. This corresponds to $Re_d = 1.43 \times 10^4$, based on the triangular vortex shedder bar diameter, $d$. Laser Doppler Velocimetry (LDV) measurements are carried out on the model at the same Reynolds number. Complementary LDV measurements are performed at a slightly higher $Re_D = 6.28 \times 10^4$, corresponding to $Re_d = 1.46 \times 10^4$. The results are normalized with the bulk velocity, $U_b$, to be comparable. The mean velocity profiles show excellent agreement. This shows in particular that the mapped inlet boundary condition that is applied in the LES is appropriate to achieve a fully developed turbulent flow profile, at the current Reynolds number. Also the variance of the data has an excellent agreement. There is a slight difference in the streamwise variance, which is caused by dynamic effects from the test rigs, according to spectral analysis of the experimental data. The spanwise fluctuations are investigated to highlight the possible presence of secondary vortices in the numerical and experimental results. It is shown that secondary vortices appear regularly in the experimental case and irregularly in the numerical case. This indicates that the utilization of LES with a mapped inlet boundary condition enables irregular detection of secondary vortices. The frequency content is investigated using a moving average together with a Gaussian filter. The results are post-processed utilizing Bayesian probability theory, to strengthen the resonance frequencies and suppress the noise. The resonance frequency of both the numerical and experimental cases appear within the expected theoretical range of $3.86 \leq f_{St} \leq 4.57$ Hz, based on the Strouhal number, $St = 0.26$. The frequency spectra of the experimental data contains a first harmonic, explained by the regular appearance of secondary vortices. The experimental measurement uncertainty of the reference instruments are included in the total uncertainty of the mean results. It can be concluded that both techniques are sufficiently accurate to study the investigated unsteady flow phenomena at the present Reynolds number.

**Acknowledgements**

The corresponding author would like to take the opportunity to express his gratitude towards the founders of the work, Vinnova – Swedish Governmental Agency for Innovation Systems. He is also grateful towards his employer SP – Technical Research Institute of Sweden, who has given him the opportunity to perform the present work as an industrial Ph.D. student. The simulations were performed on resources at Chalmers Centre for Computational Science and Engineering (C3SE) provided by the Swedish National Infrastructure for Computing (SNIC). A special thanks is directed towards the LDV experts at PTB, Jonas Steinbock and Martin Straka, who assisted during measurements. Also, Dr Thomas Lederer, who initiated the cooperation between SP and PTB regarding the LDV measurements, is acknowledged.

## 6. References


[1] T. von Kármán, Über den Mechanismus des Widerstandes, den ein bewegter Körper in einer Flüssigkeit erfährt, Göttinger Nachrichten, mathematisch-physikalische Klasse (1911,1912) 509–517,547–556.

[2] G. L. Pankanin, The vortex flowmeter: various methods of investigating phenomena, Measurement Science and Technology 16, doi:10.1088/0957-0233/16/3/R01.

[3] A. Venugopal, A. Agrawal, S. Prabhu, Review on vortex flowmeter - Designer perspective, Sensors and Actuators A: Physical 170 (2011) 8–23.

[4] E. Achenbach, Distribution of local pressure and skin friction around a circular cylinder in cross-flow up to $Re = 5 \times 10^6$, Journal of Fluid Mechanics 34 (1968) 625–639.

[5] V. Hans, H. Windorfer, S. Perpeet, Influence of vortex structures on pressure and ultrasound in vortex flow-meters, in: XVI IMEKO World Congress, 2000.

[6] V. Hans, H. Windorfer, Comparison of pressure and ultrasound measurements in vortex flow meters, Measurement 33 (2003) 121–133, doi:10.1016/S0263-2241(02)00057-X.

[7] H. Zhang, Y. Huang, Z. Sun, A study of mass flow rate measurement based on the vortex shedding principle, Flow Measurement and Instrumentation 17 (2006) 29–38.

[8] R. Courant, K. Friedrichs, H. Lewy, Über die partiellen Differenzengleichungen der mathematischen Physik, Mathematische Annalen (1869) 32–74.

[9] L. Zou, L. Larsson, M. Orych, Verification and validation of CFD predictions for a manoeuvring tanker, Journal of Hydrodynamics, Ser. B 22 (2010) 438–445, doi:10.1016/S1001-6058(09)60233-X.

[10] J. P. Hessling, Deterministic Sampling for Propagating Model Covariance, SIAM/ASA J. UNCERTAINTY QUANTIFICATION 1 (2013) 297–318.

[11] W. S. Cleveland, Robust Locally Weighted Regression and Smoothing Scatterplots, Journal of the American Statistical Association 74 (1979) 829–836.

[12] F. M. White, Fluid Mechanics, Seventh Edition in SI Units, McGraw-Hill, 2011.

[13] C. F. Colebrook, Turbulent Flow in Pipes, with Particular Reference to the Transition between the Smooth and Rough Pipe Laws, Journal of the ICE 11 (1939) 133–156.

[14] P. Welch, The Use of Fast Fourier Transform for the Estimation of Power Spectra: A Method Based on Time Averaging Over Short, Modified Periodograms, IEEE Transactions on Audio Electroacoustics AU-15 (1967) 70–73.

[15] G. L. Bretthorst, Lecture Notes in Statisticcs, Springer-Verlag, 1988.

[16] H. H. Ferziger, M. Perić, Computational Methods for Fluid Dynamics, Springer, 3 edn., ISBN 3-540-42074-6, 2002.

[17] Open∇FOAM, Open∇FOAM, The Open Source CFD Toolbox, User Guide, URL `http://foam.sourceforge.net/docs/Guides-a4/UserGuide.pdf`, 2013.

[18] H. Versteeg, W. Malalasekera, An Introduction to Computational Fluid Dynamics, The Finite Volume Method, Pearson Education Limited, Essex, England, 2 edn., ISBN 978-0-13-127498-3, 2007.

[19] R. I. Issa, Solution of the Implicitly Discretised Fluid Flow Equations by Operator-Splitting, Journal of Computational Physics 62 (1986) 40–65.

[20] S. V. Patankar, D. B. Spalding, A Calculation Procedure for Heat, Mass and Momentum Transfer in Three-dimensional Parabolic Flows, International Journal of Heat and Mass Transfer 15 (1972) 1787–1806.

[21] J. Smagorinsky, General Circulation Experiments with the Primitive Equations, Monthly Weather Review 91 (3) (1963) 99–164.

[22] M. Rudman, H. M. Blackburn, Large Eddy Simulation of Turbulent Pipe Flow, in: Second International Conference on CFD in the Minerals and Process Industries, Australia, 503–508, 1999.

[23] J. G. M. Eggels, F. Unger, M. H. Weiss, J. Westerweel, R. J. Adrian, R. Friedrich, F. T. M. Nieuwstadt, Fully developed turbulent pipe flow: a comparison between direct numerical simulation and experiment, Journal of Fluid Mechanics 268 (1994) 175–209.

[24] Air-Cooled Ion Lasers Operating Manual, Series 543 and Series 643, Melles Griot, Carlsbad, California, 1999.

[25] Scattered Light Separation and Photodetector System Model PDM, TSI Incorporated, USA, 2012.

[26] Working Group 1 of the Joint Committee for Guides in Metrology (JCGM/WG 1), Evaluation of measurement data — Guide to the expression of uncertainty in measurement, 2008.

[27] ITTC, Recommended Procedures and Guidelines, Uncertainty Analysis Laser Doppler Velocimetry Calibration, 7.5-01-03-02, in: International Towing Tank Conference, 2008.

[28] J. Hunt, A. Wray, P. Moin, Eddies, Streams, and Convergence Zones in Turbulent Flows, in: Center for Turbulence Research, Proceedings of the Summer Program, 1988.